



Cold Spray and Laser-Assisted Cold Spray of CrMnCoFeNi High Entropy Alloy Using Nitrogen as the Propelling Gas

Roghayeh Nikbakht¹ · Cristian V. Cojocaru² · Maniya Aghasibeig² ·
Éric Irissou² · Taek-Soo Kim³ · Hyoung Seop Kim⁴ · Bertrand Jodoin¹

Submitted: 8 October 2021 / in revised form: 24 January 2022 / Accepted: 5 February 2022 / Published online: 9 March 2022
© ASM International 2022

Abstract The cold spray deposition behavior of a CrMnCoFeNi High Entropy Alloy (HEA) powder was investigated using N₂ as the process gas on three different substrates of Al6061, mild steel and Hastelloy X. Well adhering and dense coatings were obtained at 950 °C and 5 MPa of propelling gas temperature and pressure, respectively. Microstructure and microhardness analyses showed significantly deformed particles in dense coatings on all three substrates, with imperfect inter-particle bonding. Laser-assisted cold spray (LACS) was used to enhance the deposition behavior of the CrMnCoFeNi powder and inter-particle bonding. Electron channeling contrast imaging analyses of coatings showed that linear structures similar to

twinning are formed in the deposited particles. X-ray diffraction analysis showed that the single-phase face center cubic structure of CrMnCoFeNi powder is retained in the coatings, although peak broadening associated with grain refinement was observed. Comparison of the physical parameters (i.e., particle velocity and temperature at impact) required for deposition of CrMnCoFeNi powder with those required for conventional alloys revealed that the deposition of this HEA is significantly more challenging due to solid solution strengthening and excellent work hardenability.

Keywords bonding · CrMnCoFeNi high entropy alloy · cold spray · impact temperature and velocity modeling · laser-assisted cold spray · microstructure evolution

This article is part of a special topical focus in the Journal of Thermal Spray Technology on High Entropy Alloy and Bulk Metallic Glass Coatings. The issue was organized by Dr. Andrew S.M. Ang, Swinburne University of Technology; Prof. B.S. Murty, Indian Institute of Technology Hyderabad; Distinguished Prof. Jien-Wei Yeh, National Tsing Hua University; Prof. Paul Munroe, University of New South Wales; Distinguished Prof. Christopher C. Berndt, Swinburne University of Technology. The issue organizers were mentored by Emeritus Prof. S. Ranganathan, Indian Institute of Sciences.

✉ Roghayeh Nikbakht
roghayeh.nikbakht@uottawa.ca

- ¹ Department of Mechanical Engineering, University of Ottawa, Ottawa, ON, Canada
- ² National Research Council of Canada, Boucherville, QC, Canada
- ³ Korea Institute of Industrial Technology (KITECH), Korea Institute for Rare Metal, Goryeong-gun, Republic of Korea
- ⁴ Department of Materials Science and Engineering, Pohang University of Science and Technology (POSTECH), Pohang, Republic of Korea

Introduction

Surface properties of materials are of utmost importance for their performance in different applications. Different types of coatings are applied to the surfaces of different components of industrial parts to enhance their performance, such as thermal insulation for high-temperature applications in the aerospace sector (Ref 1), abrasion resistant coatings for rotating components (Ref 2), and highly corrosion and oxidation resistant coatings for various gaseous and corrosive atmospheres (Ref 3). However, not many coating candidates exist for long-term protection of certain metallic parts when used in harsh conditions, such as under impact and instantaneous loading conditions, and cryogenic applications. Materials for such applications need a new material design concept with optimum strength and toughness (Ref 3, 4). High entropy alloys (HEAs) are a new class of emerging materials with four or more alloying

elements and are promising candidates for these applications. In contrast to the traditional alloys with compositions close to the corner of the phase diagrams, i.e., few percent of alloying elements added to a base element, HEAs are close to the center of the phase diagrams with multiple principal alloying elements, thereby so-called multi-principal alloys (Ref 5). CrMnCoFeNi, also Oknown as Cantor alloy, is a HEA with a single-phase solid solution and an fcc crystal structure that presents a unique combination of strength and ductility that makes it suitable to be used under impact loading and cryogenic conditions (Ref 6, 7).

HEA coatings including metallic, ceramic (Ref 8, 9) and composite coatings (Ref 4, 10) have been produced using different laser-based cladding, chemical vapor deposition and thermal spray methods (Ref 3, 4). Among different coating methods, cold spray (CS), a process part of the thermal spray family, offers the advantage of a fast and cost-effective solid-state production technique for the deposition of metallic and composite coatings capitalizing on minimal oxidation and melting-related problems (Ref 11–15).

In CS, a compressed gas is expanded/accelerated through a de-Laval-type nozzle to supersonic velocities. The feedstock powder is fed to the gas stream either upstream (high pressure) of the nozzle throat or downstream (low pressure) and propelled toward the substrate at high kinetic energy and relatively low thermal energy, compared to the other thermal spray methods (Ref 16–20). Powder particles bond to the substrate if their impact velocities reach and exceed a material-dependent critical velocity (Ref 20, 21). Usually, nitrogen (N_2) or air is used as propellant gas for cost-effectiveness; however, helium (He) can be used to provide higher particle impact velocity, yielding higher deposition efficiency and coating density. A recent research study has shown that severe plastic deformation can enhance the impact and energy absorption of CrMnCoFeNi HEA by formation of stacking faults, twins, fcc to hcp phase transformation, and amorphization (Ref 7). Therefore, CS coatings which typically are formed under a high strain rate, cold and severe plastic deformation (Ref 14) could enhance the resistance of the alloy in extreme loading conditions and the energy absorption capacity of CrMnCoFeNi HEA coatings/parts.

CS is successfully used for deposition of pure elements (Ref 11, 12, 14), composite materials (Ref 13, 15), some Al and Ti alloys (Ref 22–25), and on fewer occasions stainless steel (Ref 26–30) and Inconel 718 superalloys (Ref 31). CS of HEAs has been limited to few studies on the deposition of CrMnCoFeNi HEAs (Ref 32–35). Yin et al. (Ref 32), Xu et al. (Ref 33) and Ahn et al. (Ref 34) initially demonstrated the possibility of depositing CrMnCoFeNi by CS when He was used as the process gas. Yin et al. (Ref 32) reported incomplete interparticle bonding even when using

He at gas temperature (T_{gas}) of 300 °C and gas pressure (P_{gas}) of 3.0 MPa. In a previous work (Ref 35), the bonding mechanisms of CrMnCoFeNi HEA were studied in detail by single powder particle impact using a low-pressure cold spray (LPCS) system and using both He and N_2 as process gases on pure nickel, stainless steel 304 (SS304) and Inconel 625 substrates (Ref 35). The successful deposition of single particles was achieved only with the use of He (T_{gas} and P_{gas} of 400 °C and 3.2 MPa, respectively), while using N_2 as the process gas did not result in coating buildup even at maximum spray parameters of the employed CS system (T_{gas} and P_{gas} of 3.4 MPa and 500 °C, respectively).

As He is an expensive non-renewable and scarce source, its use on an industrial scale is limited and the use of N_2 as the propelling gas is preferred for a sustainable development of HEA CS coating deposition. The results of preliminary studies showed that deposition of CrMnCoFeNi is challenging mainly due to excellent strain hardening rate and low thermal softening, leading to a high critical velocity of deposition which was not achievable when using spray parameters usually available in commercial LPCS equipment (Ref 35). Therefore, this work aims to study the CS deposition of CrMnCoFeNi HEA using high-pressure CS equipment (HPCS). N_2 is used as the process gas to explore its potential to produce HEA coatings for industrial use. HPCS should lead to higher particle impact velocities and temperatures. The critical velocity depends on different parameters including the temperature of the impacting particles, which is controlled by the process parameters, in addition to the thermo-mechanical properties of the particles (Ref 15, 36). Therefore, understanding of the process parameters-microstructure relationship is required to optimize the deposition process (Ref 15, 21).

Particle/substrate surface temperature is also a factor influencing particle deposition (Ref 37). Different methods including substrate heating (Ref 38), particle heating, laser pre-treatment and laser-assisted cold spray (LACS) (Ref 39) have been used to improve the CS process performance. In LACS material deposition and coating buildup are promoted by laser heating of the deposition zone. The LACS process has been successfully used for the deposition of different materials including Ti-6Al-4V (Ref 40) and MCrAlYs (Ref 41).

In this work, CS and LACS processes were employed for the deposition of CrMnCoFeNi HEA coatings. The coatings were deposited on three different substrates including Al6061 alloy, mild steel 1020 and Hastelloy X nickel-based superalloy. As the critical velocity of CrMnCoFeNi HEA has never been reported, simulations to obtain the particle impact velocity (V_p) and temperature (T_p) are performed to correlate their effects on the deformation and deposition behavior of this HEA powder and were compared to spray parameters of SS304 coatings

deposited by CS, which has a similar range of mechanical and physical properties to CrMnCoFeNi HEA. A few different coatings were sprayed using a matrix of different spray parameters. The coatings characteristics and microstructures were evaluated. The phase structures of the CS and LACS CrMnCoFeNi coatings were investigated using x-ray diffraction. The mechanical properties of the deposited coatings were assessed using microhardness testing.

Experimental Procedures

Powder and Substrates

The feedstock CrMnCoFeNi HEA powder was atomized in-house from a master alloy (Ref 35, 42). The atomized powder was sieved and particles with diameters of less than 60 μm were used. The powder particle size distribution was measured by a laser diffraction particle size analyzer (LS320, Beckman Coulter, USA). Al6061 alloy, mild steel and Hastelloy X substrates ($\text{\O}25.4 \times 3.175$ mm) were grit blasted using alumina grit and were used for CS deposition. The roughness of the substrates was measured using a profilometer (Mitutoyo SJ-201 stylus profilometer) and an average of 5 measurements was reported.

Cold Spray Deposition

A commercially available HPCS system, PCS-1000 (Plasma Giken, Japan), was used for the deposition process. Coatings were deposited by varying few spray parameters: powder feed rate, gun traverse speed and the number of passes while maintaining the propelling gas stagnation temperature and pressure and standoff distance constant at 950 $^{\circ}\text{C}$, 4.9 MPa and 50 mm, respectively. The spray parameters together with the coating identifications (ID) to be used throughout the paper are provided in Table 1.

Laser-Assisted Cold Spray Deposition

In order to improve the inter-particle bonding of the CrMnCoFeNi HEA, a LACS setup composed of a 4 kW fiber laser (1064 nm wavelength, IPG Photonics, USA) was used. The laser was operated in the continuous wave mode and the laser spot preceded the spray jet on the surface of the substrate. The LACS coatings were deposited on mild steel substrates using the spray parameters presented in Table 1.

Characterization

Microstructural characterization of the feedstock powder and deposited coatings were performed using a scanning electron microscopy (SEM) (EVO-MA10, Zeiss, Germany) and a field emission SEM (Gemini 500, Zeiss, Germany) equipped with secondary electron (SE), backscattered electron (BSE) and energy-dispersive spectroscopy (EDS). The cross sections of the coatings were prepared using standard metallographic techniques (ASTM E1920-03) for microstructural analysis. The characterization of the powder and coating microstructures were performed using the electron channeling contrast imaging (ECCI) method. Using this method, microstructure analyses can be performed on bulk samples/coatings where crystalline defects can be imaged with a visibility depth of about a hundred nanometers below the surface, which is in the same order of magnitude as the thickness of a Transmission Electron Microscope (TEM) thin foils. Furthermore, this method allows getting TEM-like contrasts from bulk samples (Ref 43). Microstructural features such as particle deformation, inter-particle bonding, substrate/coating interface morphology, coating thickness and microstructure evolution from powder particles to deformed particles in coatings were obtained from the polished coatings cross-sectional images.

A diffractometer (D8-Discovery, Bruker AXS Inc. Madison, WI, USA) in Bragg-Brentano (θ - 2θ) configuration was used to analyze the phase composition of the powder and coatings. The diffracted signal was collected over a two-theta range of 10° - 90° with a step size of 0.02°

Table 1 The CS and LACS parameters for deposition of CrMnCoFeNi coatings on Al6061, mild steel and Hastelloy X substrates

Coating ID	T_{gas} , $^{\circ}\text{C}$	P_{gas} , MPa	Traverse speed, mm/s	Feeding rate, g/min	Number of passes	Laser power, kW
CS ₁			200	24	3	...
CS ₂			200	12	4	...
CS ₃	950	4.9	100	12	3	...
CS ₄			400	12	6	...
LACS			100	12	3	1

and a 5 sec/step acquisition time through a 1° fine collimator slit.

Vickers microhardness tests were performed on the cross sections of the substrates, powder and coatings to evaluate particle deformation. Microhardness analyses were conducted using 10, 25, 50 and 300 gf loads and a dwell time of 10 s using a microhardness tester (Duramin-1, Struers Inc., Cleveland, OH, USA). The reported values are the average of 10 indentations for each sample, taken from random locations on the polished samples.

Particle Impact Velocity and Temperature Simulations

Impact velocity and temperature of the CrMnCoFeNi particles were simulated for the spray condition of P_{gas} 4.9 MPa, T_{gas} 950 °C and a 50 mm standoff distance. To better understand the effect of particle velocity and temperature on its deposition, the simulation results were compared to those obtained for the spray conditions used in previous work with the LPCS system (P_{gas} of 3.2 MPa, T_{gas} of 400 °C and 30 mm standoff distance, using He as well as P_{gas} of 3.4 MPa, T_{gas} of 500 °C and 30 mm standoff distance, using N₂). To ensure accurate particle tracking, the complete flow profiles from the nozzle inlet up to the substrate surface are determined. The 2D axisymmetric compressible flow simulations are carried out using SU2, an open-source multi-physics and design software. This is followed by the particle tracking simulations carried out using the one-way coupled particle computational fluid dynamics (CFD) module of the CSAM Digital Solutions software (NRC, Canada). The full effect of the substrate on the flow and consequently the influence of the bow shock on particle trajectory are considered in the simulations. Governing equations, their numerical discretization and the core elements of particle tracking were detailed in a previous publication (Ref 44).

Results and Discussion

Powder Characteristics

SEM micrograph of the free-standing CrMnCoFeNi powder in Fig. 1(a) shows that the powder has a spherical morphology. The ECCI analysis of the powder particles cross section in Fig. 1(b) and (c) demonstrates that particles have cellular (dendritic) microstructure with relatively large grains, which are also visible on the inset image of Fig. 1(a) from the surface morphology of the powder particle. Microstructure varieties can be seen from the cross section image of the particles in Fig. 1(b) for different size

particles. The powder particle size distribution in Fig. 1(d) shows a three-peak Gaussian distribution of the particles with a D_{10} value of 9.5 μm, a D_{50} value of 25.5 μm, and a D_{90} value of 44.6 μm. The EDS spectrum of the powder (Fig. 1e) confirms that the powder composition is very close to equiatomic composition.

The XRD analysis of the powder in Fig. 2 has three main peaks on (111), (200) and (220) planes, which are characteristic of a single-phase face-centered cubic (fcc) structure. The elemental map distributions and composition of the powder have already been reported (in (Ref 35)), confirming that the composition of the powder is very close to equiatomic composition and elements are distributed homogeneously without visible segregation.

Coatings Characteristics and Microstructure

Cross section images of the CS₁, CS₂, CS₃ and CS₄ coatings are presented in Fig. 3. It can be seen that the HEA powder was successfully deposited on all three substrates—from soft to hard; i.e., Al6061, mild steel and Hastelloy X substrates with measured hardness values of 104, 204 and 236 HV_{300gf}, respectively (Table 2)—at all selected spray parameters.

Comparison of the coatings shows that the coatings deposited on the soft Al6061 substrates exhibit a different interface morphology compared to those deposited on mild steel and Hastelloy X. The coating/substrate interface morphologies have wavy profiles with amplitudes being close to ≈ 10 μm when deposited on the hard substrates (mild steel and Hastelloy X substrates), while the amplitude is in the range of ~ 45 μm for the coating/Al6061 interfaces. The roughness values of the two hard substrates (Table 2) changed slightly by impact of the bounced off particles and shallow penetration of the deposited ones while for the softer Al substrates this value changed significantly (from 4.68 to 45 μm). Additionally, particle boundaries mostly are visible within the coatings because of the imperfect bonding of the HEA particles. Higher magnification images of the HEA/Al6061 interfaces in Fig. 4 demonstrate that the first layer of impacting HEA particles penetrated and embedded in the Al6061 substrate without significant deformation as the spherical morphology of the deposited powder particle is discernible from the image, whereas the successive impacted particles experienced more deformation.

Figure 5 compares the thickness of the coatings sprayed on different substrates for each cold spray condition. The thickness of the coatings varies between approximately 80 and 250 microns where the thickest coatings were achieved for CS₃ deposited on Al6061 and mild steel. Considering the spraying parameters of Table 1, for the same number of passes the powder quantity projected on the substrates

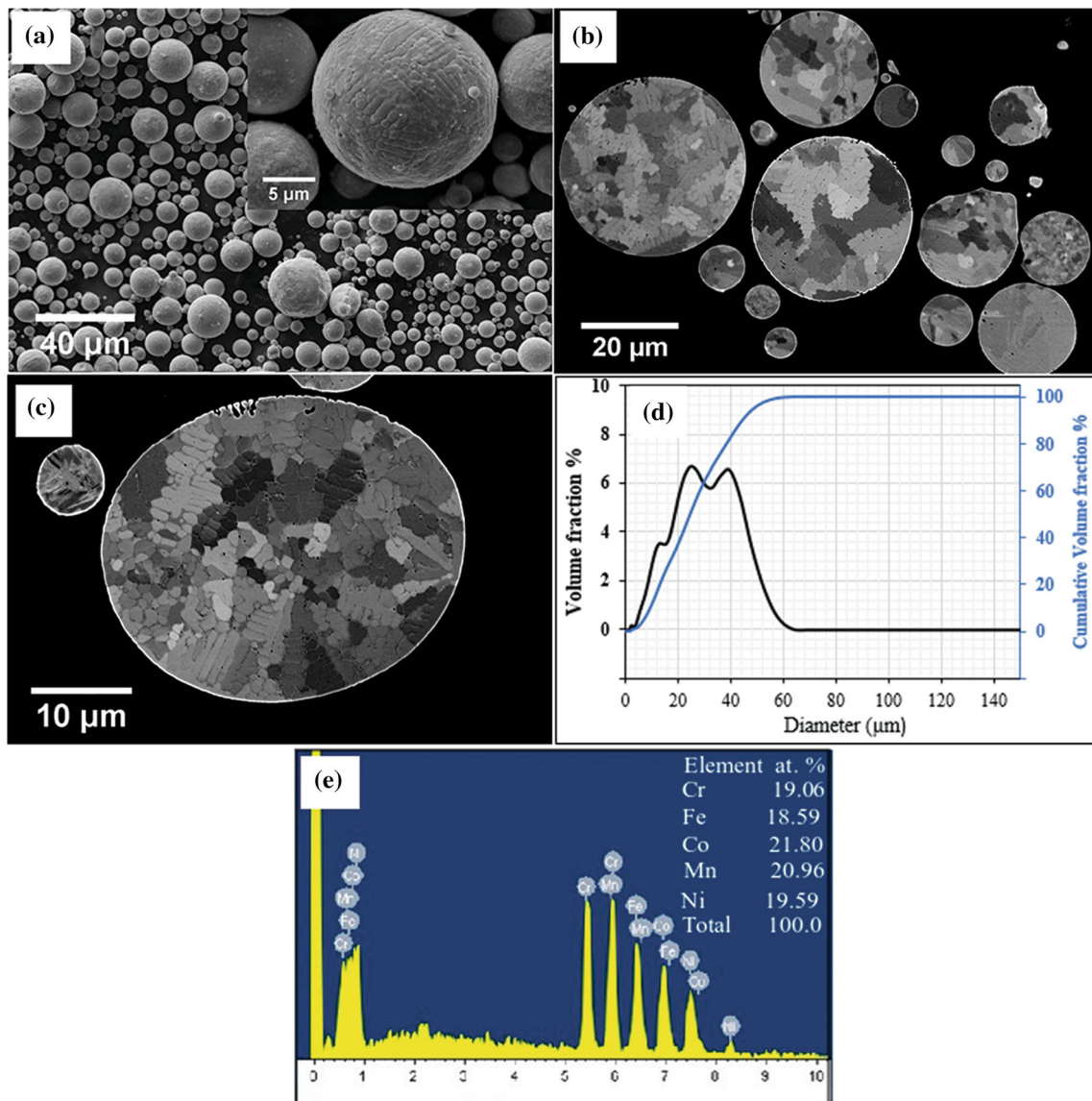


Fig. 1 High entropy CrMnCoFeNi powder characteristics. (a) SEM micrograph of free-standing powder shows that the powder has a spherical morphology, (b) and (c) ECCI analysis of the powder cross

section reveals the cellular (dendritic) grain distribution, (d) measured powder particle size distribution, $D_{10} = 9.5 \mu\text{m}$, $D_{50} = 25.5 \mu\text{m}$ and $D_{90} = 44.6 \mu\text{m}$, and (e) EDS spectrum of the powder

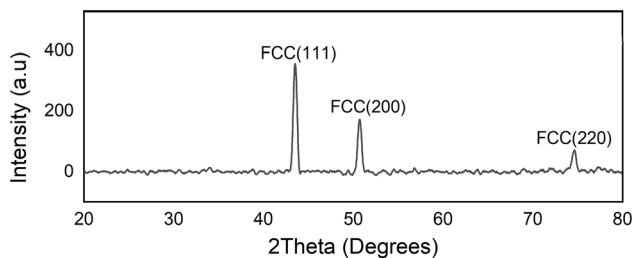


Fig. 2 XRD analysis of the atomized CrMnCoFeNi HEA powder illustrates that the powder is single phase and has fcc crystal structure

(feeding rate/traversing speed) for CS_1 and CS_3 conditions were equal; however, CS_3 coating—specifically on mild steel substrate—with a lower traverse speed and therefore a

higher surface temperature has a higher thickness. Therefore, the relatively higher deposition rate of CS_3 coating can be related to the surface temperature effect, which seems to be more significant when spraying on the mild steel substrate. Fig. 6 compares coatings deposited on Al6061 substrates using CS_1 and CS_3 spraying parameters. The CS_3 coating not only is thicker but also has a better coating quality as particle boundaries are less visible, which can be also attributed to the relatively higher surface temperature associated with the lower gun traverse speed, promoting particle adhesion.

On the other hand, considering the powder quantity sprayed on each surface (normalized by the spray condition of CS_1 coating: $CS_1 = 1$, $CS_2 = 0.67$, $CS_3 = 1$ and $CS_4 =$

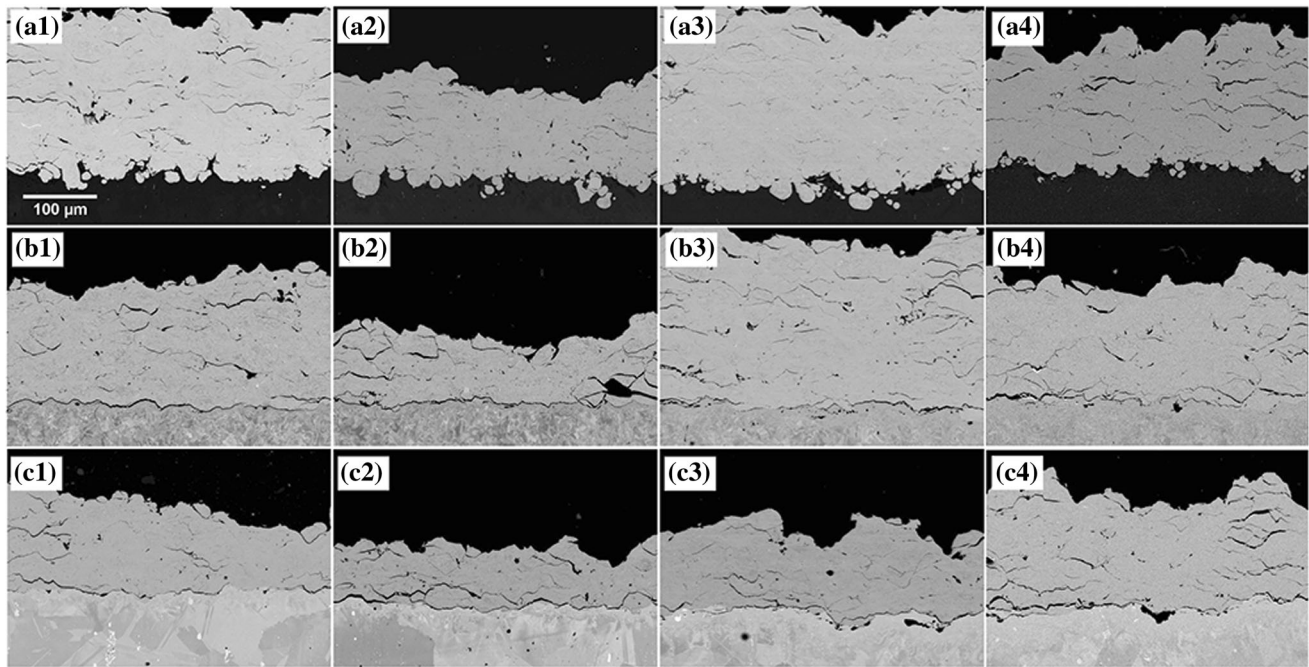


Fig. 3 CrMnCoFeNi HEA coatings cross section images on three substrates (same magnification for all micrographs). (a1–a4) CS₁, CS₂, CS₃ and CS₄ coatings deposited on Al6061, (b1–b4) CS₁, CS₂, CS₃

and CS₄ coatings deposited on mild steel, and (c1–c4) CS₁, CS₂, CS₃ and CS₄ coatings deposited on Hastelloy X substrates

Table 2 Measured roughness (after grit blasting) and hardness values of the substrates (the values show an average of 10 measurements per sample)

Substrates	Al6061	Mild steel	Hastelloy X
R _a , μm	4.68±0.16	3.70±0.19	2.72±0.22
Hardness, HV at 300gf	104±1.9	204±2.36	236±0.85

0.5) the thicknesses of CS₄ coatings were expected to be half of that of CS₁ and CS₃ coatings; however, the thicknesses of the CS₄ coatings are comparable with CS₁ and slightly thinner than CS₃ (Fig. 3 and 5). Furthermore, the roughness profiles of the CS₁ and CS₃ coatings in Fig. 6 demonstrate that the top surface of coatings has lots of peaks and valleys. The distance between peaks and valleys for both coatings was measured in a few spots of the profiles. The average distance between peaks and valleys is approximately in a range of 100–110 μm—while the average particle size is approximately 25 μm. Such surface profiles were observed for the other coatings as well with the approximately same average values of 100 μm. This high surface roughness of coatings and relatively large standard deviation of coatings thickness combined with the appearance of coatings top surface supports the notion that some chunks of deposited particles were eroded from the surface of the coating upon nozzle traverse in the successive passes. Consequently, it is hypothesized that the

higher deposition rate of CS₄ coatings compared to CS₁ and CS₃ is related to its higher traverse speed which potentially can reduce the erosion effect as suggested in the literature (Ref 45).

Therefore, one can conclude that traverse speed influences the deposition rate of the HEA coatings by two opposite effects: (i) increase in deposition rate by increase in surface temperature at lower traverse speed, (ii) decrease in deposition rate by an increase in erosion. Although the differences in traverse speed are not very drastic in these experiments, the erosion of the particles (as shown in the surface profile of the coatings in Fig. 6) seems to play a role because of the relatively poor bonding of the HEA particles. Therefore, based on these findings, a combination of lower traverse speed with lower feeding rate (CS₃ compared to CS₁) and/or higher traverse speeds at fixed feeding rates (CS₄ compared to CS₃) result in a higher deposition rate of HEAs where the former related to the effect of temperature in lower traverse speed and the latter is potentially related to lower erosion at higher traverse speeds.

A close look at the microstructure of the coatings in Fig. 3 and 4 shows that inter-particle boundaries are mostly visible in the coating, while the particles were deformed and filled inter-particle gaps with a very low amount of porosity in the microstructure. The cross section images of a CS₁ coating on mild steel and Hastelloy X substrates in Fig. 7 show the presence of well deformed and flattened

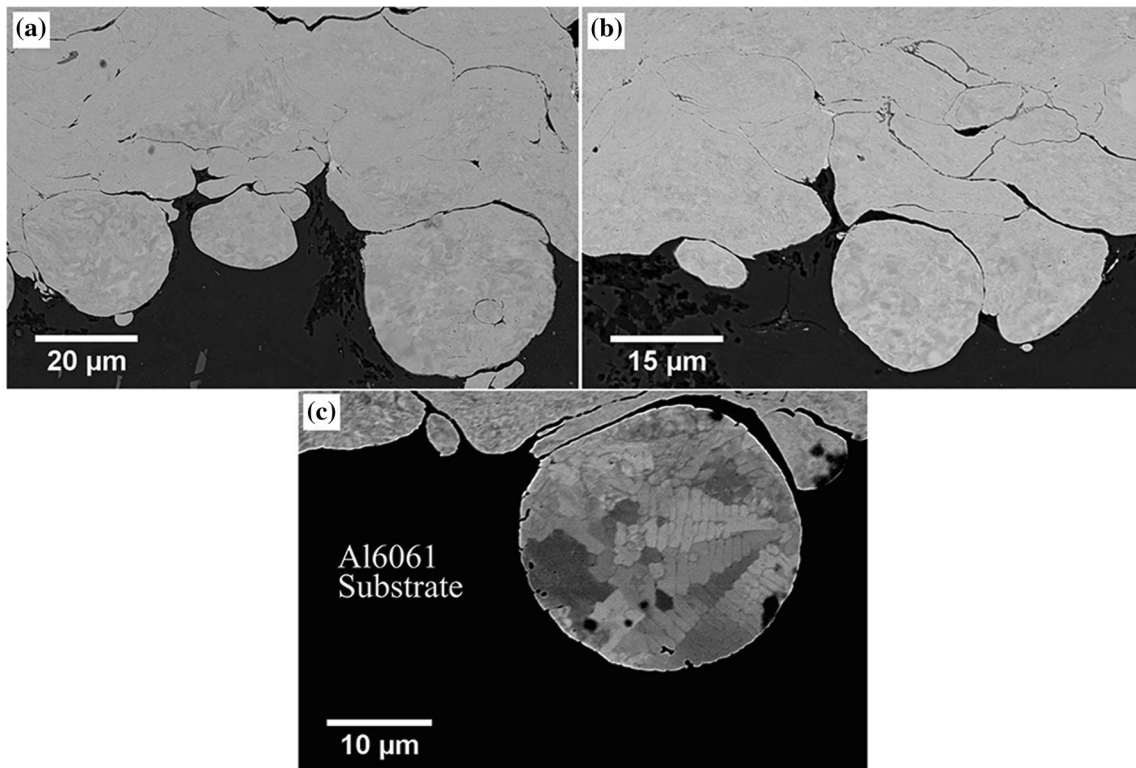


Fig. 4 ECCI images of the CrMnCoFeNi HEA coating/Al6061 interfaces show that the particles are mostly embedded in Al substrate and in most cases, the spherical shape of the first layer of the particles is discernible from the cross section images

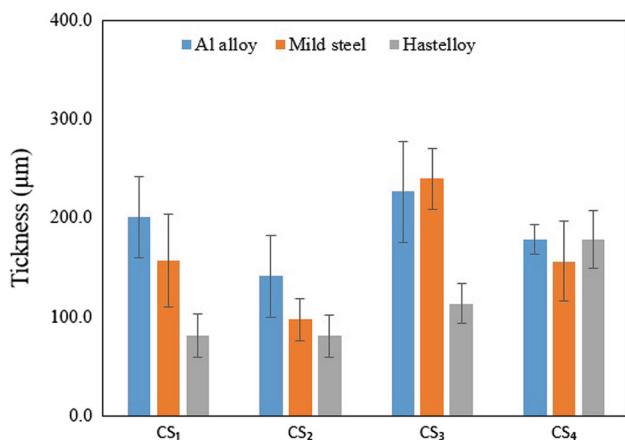


Fig. 5 Effect of spraying parameters on the thickness of the coating. The total amount of powder projected on the substrates for each spray condition was normalized with the spray conditions of CS₁ (feeding rate, traverse speed and the number of passes), and is calculated to be CS₁ = 1, CS₂ = 0.67, CS₃ = 1 and CS₄ = 0.5

HEA particles in the coating. ECCI maps illustrate severe plastic deformation at particle boundaries—but not limited to those areas—as typical of CS coatings. Additionally, bright spots can be seen at the (central) internal part of deposited particles showing high dislocation density and misorientation inside the particles. This means that the inner grains of particles experienced significant

deformation in addition to the particles’ boundaries. Despite this significant deformation, the ECCI maps of the coatings in Fig. 7(a)-(b) demonstrate that perfect bonding was not achieved at some inter-particle boundaries. The higher magnification images of the selected areas of Fig. 7(b) are shown in Fig. 7(c)-(d), which illustrate two examples of inter-particle boundaries (dashed line in Fig. 7c) and inner-particle misorientation (outlined area in Fig 7d). Elongated linear structures can be seen at the center of the particles of Fig. 7(d)-(f), which are outlined with yellow dotted lines and are similar to deformation twinning, specifically at Fig. 7(f). The deformation twinning has been reported for the single-particle impact of this powder (Ref 35), other dynamic and quasi-dynamic deformation of CrMnCoFeNi HEA (Ref 6, 7, 46, 47), and also CS deposit of pure elements (Ref 14, 48). Deformation twinning increases the strain hardening and strain hardening rate of this alloy. As reported in the literature, the solid solution strengthening and sluggish diffusion of this alloy results in low thermal softening (Ref 6, 49). The high strain hardening and low thermal softening result in a high shear localization strain. In previous work (Ref 35), it has been shown that the difficulty of deposition of HEA alloys is related to their high shear localization strain.

Findings from deposition characteristics and microstructure analyses of CS coatings (Fig. 3 and 7)

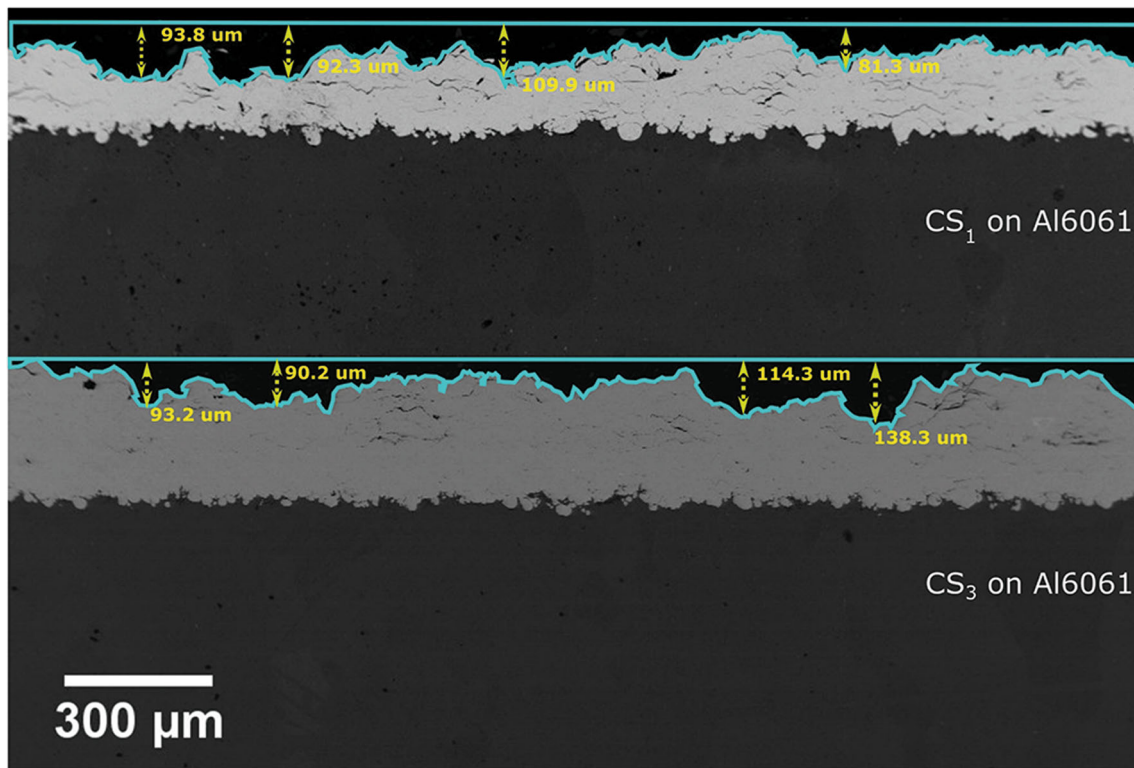


Fig. 6 Roughness profiles of the top surface of CS₁ and CS₃ coatings deposited on Al6061 substrates. The average distance between peaks and valleys is approximately 100 microns

demonstrate that the increase in impact velocity and temperature can further enhance particle bonding. As the spray parameters were close to the limitation of the employed HPCS system, LACS deposition was used to enhance the CrMnCoFeNi coatings deposition and quality. ECCI maps of LACS are presented in Fig. 8. The ECCI maps show that the deposited particles deformed more significantly compared to the CS coatings. Higher magnification images of the microstructure in Fig. 8(b) and (c) reveal that particle boundaries were forged tighter and the quality of particle bonding improved. The LACS configuration allows for localized surface (substrate or pre-deposited layer) pre-heating promoting their adhesion to the surface. As it has been shown in the previous work (Ref 35), this alloy has a relatively high strain hardening rate and lower thermal softening rate compared to pure elements such as Ni and conventional alloys such as stainless steel 304, and Inconel 625. Therefore, an increase in temperature with softening effect enhances the deformation and bonding in this alloy. Nevertheless, very high laser power at LACS deposition may result in some oxidation while the findings of this study confirm that the optimized LACS process can effectively enhance the HEA coating deposition and inter-particle bonding (Fig. 8c).

Microhardness analyses were performed to explore and compare mechanical properties of CS₃ and LACS coatings

deposited using the same spray parameters, and the results are presented in Table 3. The influence of indentation load on both CS and LACS coatings is observed in the values depicted in Table 3 with average values ranging from 361 HV to 394 HV at 100gf. It can be seen from the results that the microhardness was increased from 166 HV_{10gf} for the atomized powder to 361 and 391 HV_{100gf} in CS and LACS coatings, respectively, which confirms that particles significantly hardened in both coatings with the hardness of the LACS coating being slightly higher than that of the CS₃ coating. The increase in hardness in both coatings can be related to the high density of dislocations, defects and potentially grain refinement in the microstructure. Relatively higher hardness values were achieved for both CS₃ and LACS coatings using lower indentation loads (10–50 gf) which can be attributed to the indentation size effect as a result of visual acuity, focusing of the image) and material factors including heterogeneity of the deformation and grains size and orientation (Ref 50).

EDS maps of the coating (Fig. 9b–f) demonstrate that after LACS deposition, the distributions of all five alloying elements are homogeneous with no segregation, localization or change of composition

The XRD analyses of the CS₃ and LACS coatings in Fig. 10 demonstrate that fcc single-phase structure of the CrMnCoFeNi HEA powder remains unchanged with the

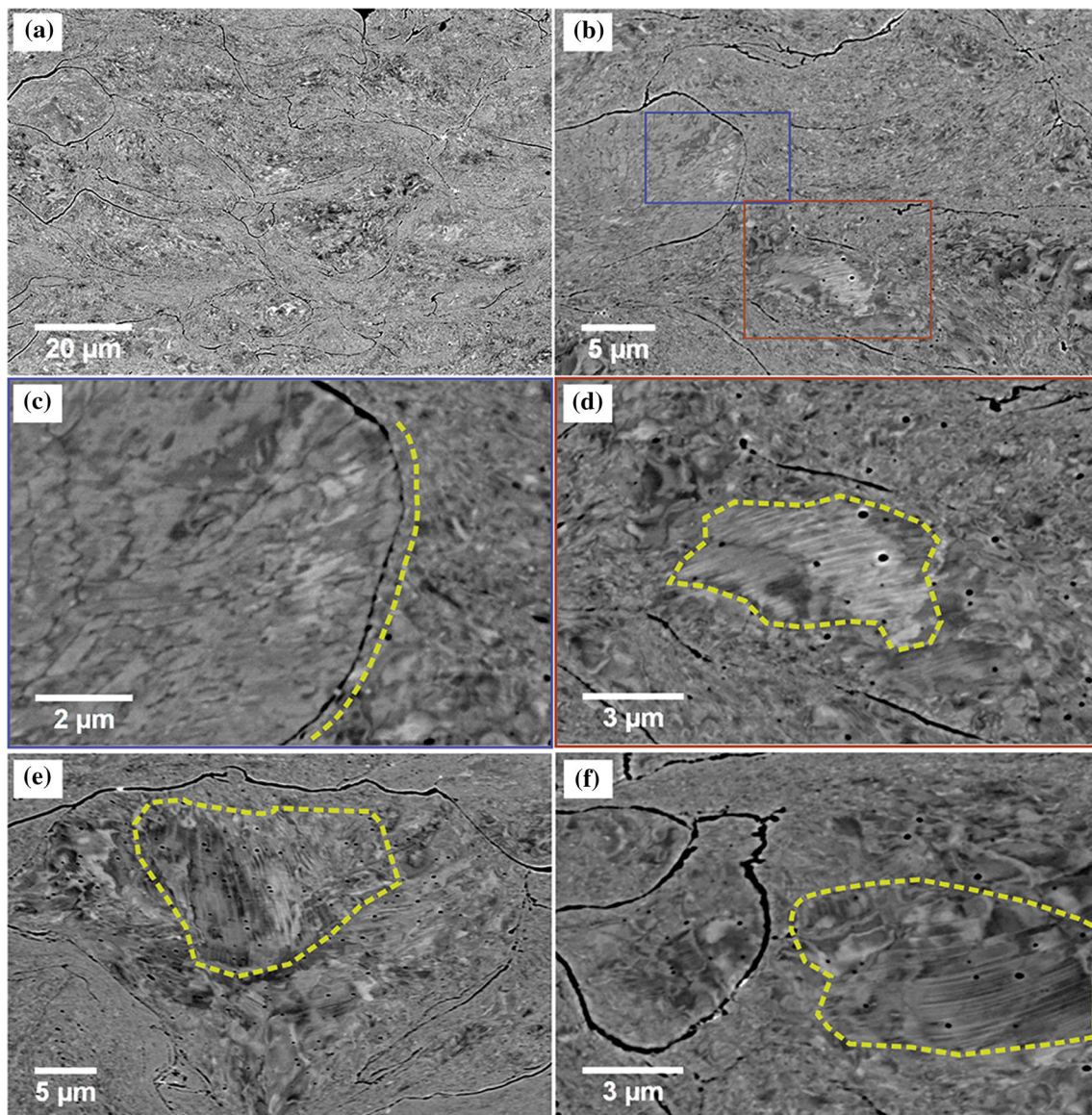


Fig. 7 ECCI images of microstructure of CrMnCoFeNi coatings. (a–b) Cross section of the CS₃ and CS₁ coating on Hastelloy X substrate at two magnifications, (c) high magnification image of the selected area of Fig. (b) illustrates that an inter-particle boundary, (d) the bright spots at the center of the particle revealing a high density of

dislocation in ECCI images (e–f) elongated linear structures with different orientations in the cross section of CS₁ coating deposited on mild steel can be seen at the center of particles in these two images which are outlined by yellow dotted lines

only difference that the (200) and (220) peaks in the coating are wider than that of the powder. Considering the fact that the full width at half maximum of a diffraction peak is wider as the crystallite size decreases (Ref 51), one can conclude that both coatings are refined during the process of deposition (Ref 14). Interestingly, (200) peak of CS coatings is relatively wider than LACS coating which means crystallite size is smaller in CS coating because of grain refinement. In CS₃, particles were deformed in a higher Zener Holman parameter (lower temperature in CS compared to LACS) which can result in dynamic recrystallization while potentially the higher temperature in

LACS can lead to dynamic recovery or static recrystallization (Ref 52).

Deposition Analyses

The simulated particle impact velocity and temperature of CrMnCoFeNi for the various spray parameters and nozzles used are presented in Fig. 11. Based on the simulation results, the average HPCS powder particle velocity and temperature at impact and the spray condition of T_{gas} of 950 °C, P_{gas} of 4.9 MPa and standoff distance of 50 mm are 726 m/s and 541 °C, respectively. Using these spraying

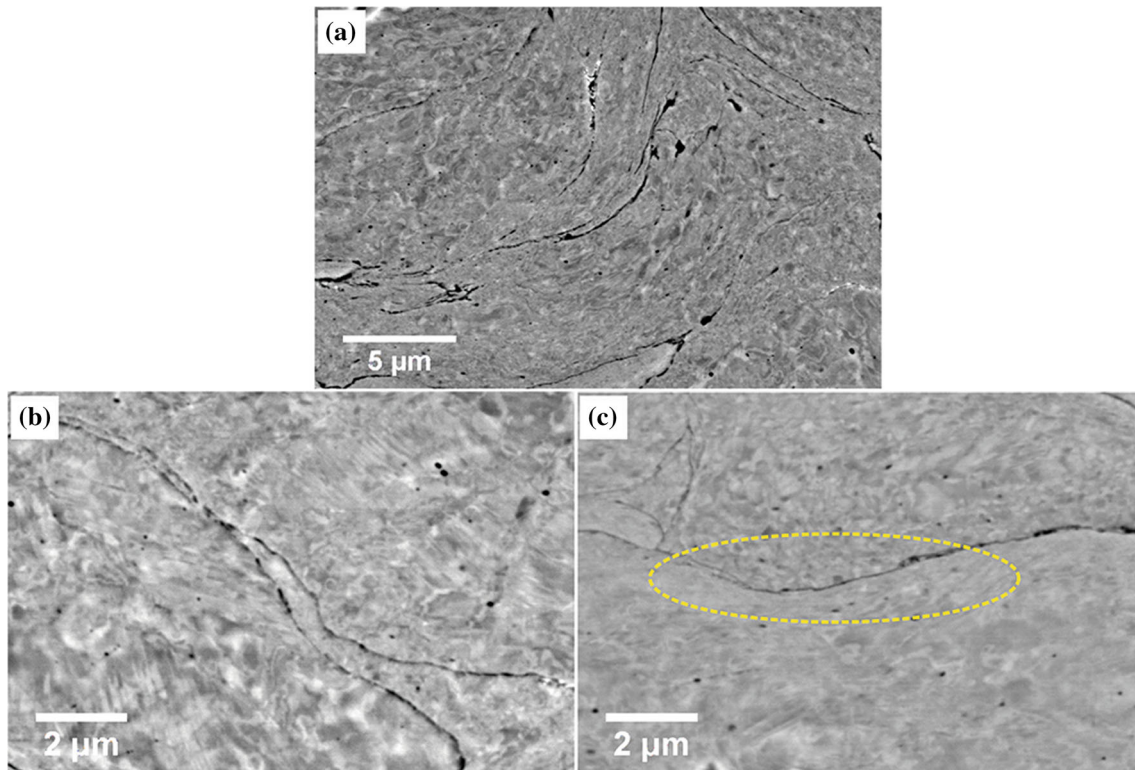


Fig. 8 ECCI maps of LACS CrMnCoFeNi HEA coatings. (a-c) Particle deformation and inter-particle bonding

Table 3 The measured microhardness of the CrMnCoFeNi HEA powder, CS and LACSHEA coatings

Sample	Load 100, gf	Load 50, gf	Load 25, gf	Load 10, gf
Powder			176±8	166±37
CS ₃	361 ± 50	397± 39	445± 46	478 ± 38
LACS	391 ± 67	394 ± 44	412 ± 131	494 ± 131

parameters, relatively dense coatings were built-up although the powder particle bonding was not perfect. In the previous work (Ref 35), the CrMnCoFeNi powder was sprayed by LPCS using He (T_{gas} of 400 °C and P_{gas} of 3.2 MPa) and N₂ (T_{gas} of 500 °C and P_{gas} of 3.4 MPa). Single particles and multi-particles were successfully deposited with He as the propellant gas while coating build-up did not occur using N₂. The impact velocity and temperature for the former spraying conditions (previous work (Ref 35)) were also simulated and are provided in Table 4. The particles' average velocity and temperature were calculated to be 811 m/s and 144 °C for the He and 560 m/s and 208 °C for the N₂ sprayed coatings (Table 4). For HPCS, the tail of the graphs (diameters <5 μm) shows the particles that are affected by the bow shock. Generally speaking, for particles with diameter <25 μm the velocity is higher with the LPCS and He, and particles with diameter >25 μm impact the substrate at similar velocities for both HPCS, N₂ and LPCS, He. There is a large difference

in particle temperature at impact between the two systems which significantly influences the particle deformation and deposition rate. The LPCS, N₂, almost for all range of particle size has the lowest V_p from the three simulated conditions with the T_p values being lower than HPCS, N₂ and higher than LPCS, He

As there are not many reports on CS of the CrMnCoFeNi HEA using N₂, the spray parameters of the HEA (Ref 32, 34) were compared to that of SS304 from the literature (Ref 27-30) (Fig. 12). From the materials properties perspective, CrMnCoFeNi HEA has a very close range of yield strength, tensile strength, density, specific heat capacity (C_p) and lower melting point compared to SS304 (Table 5). Based on the graph in Fig. 12, the successful deposition of SS304 (Ref 27-30) powder was achieved using both He and N₂ and mixed He-N₂ gas, using a range of CS parameters. Successful deposition of SS304 was reported with T_{gas} and P_{gas} of as low as 450 °C and 3 MPa using N₂ as the process gas, while successful deposition of CrMnCoFeNi alloy powder was only reported using He as the process gas with T_{gas} and P_{gas} of higher than 300 °C and 3 MPa (Ref 32, 34, 35). The current CrMnCoFeNi powder was successfully deposited using HPCS-N₂ at 950 °C and 4.9 MPa while the parameters lower than this were unsuccessful. This confirms that the CS deposition of CrMnCoFeNi HEA is more challenging compared to the conventional SS304 with almost similar materials

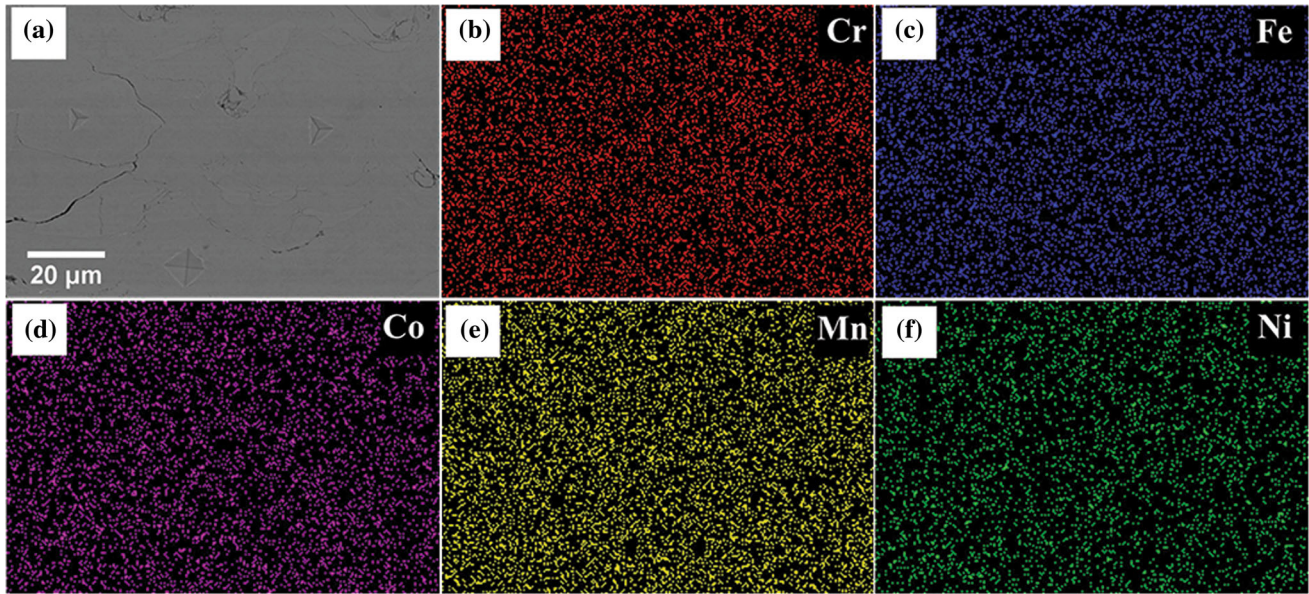


Fig. 9 Microstructure of LACS CrMnCoFeNi HEA coatings. (a) Secondary electron image of coating with two indents at two spots of the coating, and (b-f) EDS map of the coating which shows homogeneous distributions of elements in the coating

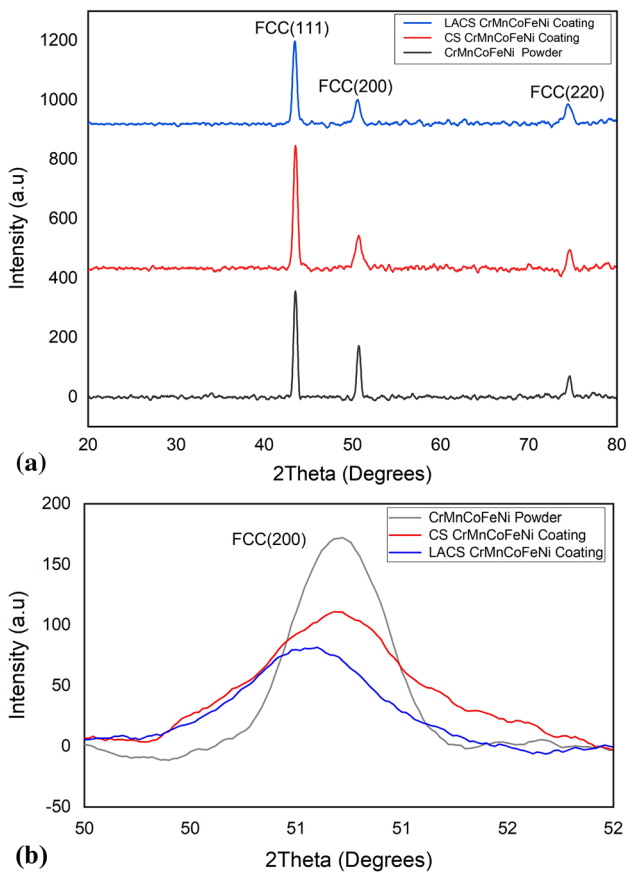


Fig. 10 (a) XRD analyses of CrMnCoFeNi HEA powder, CS₃ and LACS coatings and (b) selected area of XRD pattern of Fig (a)

properties. This can be related to the high entropy effect and solid solution strengthening mechanism of HEAs that differentiate the deformation behavior of these alloys from the conventional alloys and elements. Therefore, other material properties in addition to the yield strength, tensile strength, C_p and melting point, which are traditionally used for critical velocity calculations and deposition prediction of materials, should be considered for CS deposition prediction of the HEAs. It was shown (previous work (Ref 35)) that comparison of yield strength variation of the alloys with temperature as a measure of softening- and strain hardenability of alloys can be used as an effective measure of CS deposition prediction of the HEAs.

Comparison of the physical deposition parameters (i.e., V_p and T_p) of CrMnCoFeNi HEA at different spray conditions, deposition characteristics of the powder, top surface roughness profile of the coatings, and microstructure analyses of the coatings collectively illustrate the need for enhancing bonding quality and cohesion of the HEA coatings that could be achieved by increasing of the particle velocity and temperature at impact. LACS combines the CS process with material softening by laser and allows the HEA particles to deform and deposit at lower impact velocities compared to the conventional CS without the need of using expensive He gas. It was demonstrated that LACS process can potentially enhance the HEA deposition and improve inter-particle bonding by the addition of local heating, therefore, increasing the surface temperature and deformation and promoting better particle bonding.

Fig. 11 (a-b) Simulated V_p and T_p of CrMnCoFeNi HEA for HPCS using N_2 as the process gas at, 950 °C and 4.9 MPa, LPCS using He as the process gas at 400 °C and 3.2 MPa and LPCS using N_2 at 500 °C and 3.4 MPa

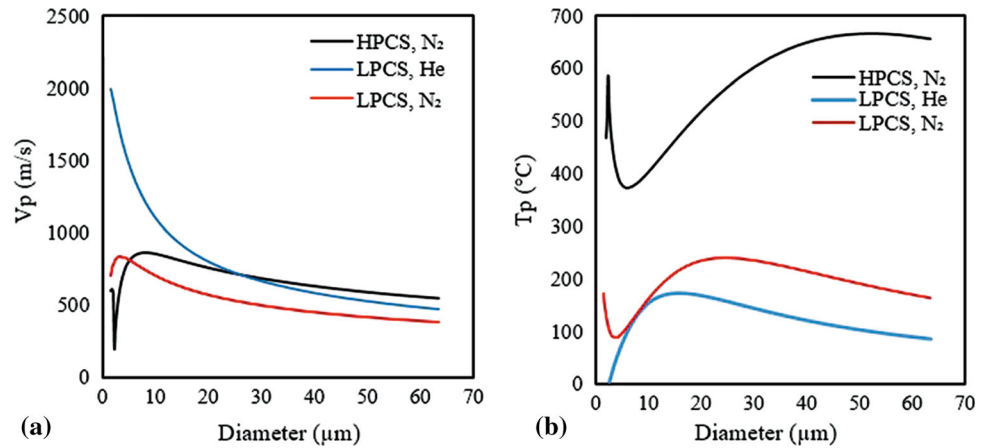


Table 4 Summary of spray conditions and simulated V_p and T_p .

Experiment	Process gas	T_{gas} , $^{\circ}\text{C}$	P_{gas} , MPa	Stand of distance, mm	V_p , m/s	T_p , $^{\circ}\text{C}$	Summary
Coating	N_2	950	4.9	50	726	541	This work-Coating build-up
Single/multi-particle	He	400	3.2	30	811	144	Previous work (Ref 35)
Coating	N_2	500	3.4	30	560	208	Previous work- No Deposition (Ref 35)

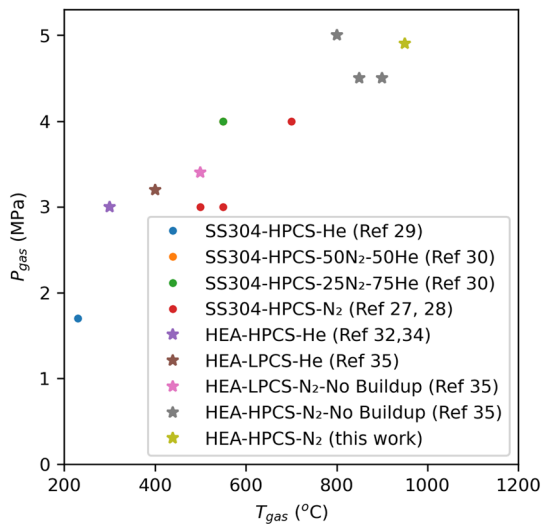


Fig. 12 Spray parameters of CrMnCoFeNi alloy from this work and literature (Ref 32, 34, 35) in comparison to spray parameters of SS304 from the literature (Ref 27-30)

Conclusion

The CS deposition behavior of a gas atomized CrMnCoFeNi HEA powder was investigated using N_2 as the process gas on three different substrates including Al6061, mild steel and Hastelloy X. LACS process was used to enhance the deposition behavior of the CrMnCoFeNi. The velocity and temperature of particles at impact were

evaluated using numerical tools and compared to the reported spray conditions of this alloy from the literature. The following results were obtained from this study:

1. CrMnCoFeNi HEA was successfully deposited using N_2 as the process gas at 950 °C and 4.9 MPa and coatings with a range of thicknesses up to 250 μm were achieved. Microstructure and microhardness analyses showed that particles significantly deformed and relatively dense coatings were achieved on all three substrates but weak inter-particle bonding within the coatings was observed. LACS process enhances the coating deposition and inter-particle bonding of CrMnCoFeNi.
2. ECCI analyses of coatings microstructures showed that linear structure similar to twinning formed at the particles, which were more visible at the inner part of the particles.
3. XRD analysis showed that the single-phase fcc phase structure of CrMnCoFeNi is retained in both CS and LACS coatings with the only difference that the peak broadening was observed for (200) and (220) peaks related to grain refinement and fine crystallite size in deposited coatings.
4. Comparison of deposition parameters of CrMnCoFeNi powder employed in this work with SS304 from the literature—which has a very close range of materials properties to CrMnCoFeNi—showed that deposition of the HEA is significantly challenging compared to

Table 5 Comparison of bulk material properties of the CrMnCoFeNi and SS304 (Ref 6, 35)

Material	Tensile strength, MPa	Yield strength, MPa	Melting point, °C	Density, g/cm ³	Specific heat, J/(kg K)
CrMnCoFeNi	491	238	1623	7.86	450
SS304	505	243	1723	8.06	490

conventional alloys due to solid solution strengthening and excellent work hardenability of this alloy.

Acknowledgement The NRC authors would like to acknowledge the support from the Materials and Processes Directorate NRC Boucheville for making this work possible.

References

- N.P. Padture, M. Gell and E.H. Jordan, Thermal Barrier Coatings for Gas-Turbine Engine Applications, *Science*, 2002, **296**, p 280–284. <https://doi.org/10.1126/science.1068609>
- R. Nikbakht, B. Jodoin, Thick Cu-hBN Coatings Using Pulsed Gas Dynamic Spray Process: Coating Formation Analysis and Characterisation, *J. Therm. Spray Technol.*, 2022. <https://doi.org/10.1007/s11666-022-01318-y>
- A. Sharma, High Entropy Alloy Coatings and Technology, *Coatings*, 2021, **11**, p 372. <https://doi.org/10.3390/coatings11040372>
- A. Meghwal, A. Anupam, B.S. Murty, C.C. Berndt, R.S. Kottada and A.S.M. Ang, Thermal Spray High-Entropy Alloy Coatings: A Review, *J. Therm. Spray Technol.*, 2020, **29**, p 857–893. <https://doi.org/10.1007/s11666-020-01047-0>
- E.P. George, D. Raabe and R.O. Ritchie, High-Entropy Alloys, *Nat. Rev. Mater.*, 2019, **4**, p 515–534. <https://doi.org/10.1038/s41578-019-0121-4>
- W. Li, D. Xie, D. Li, Y. Zhang, Y. Gao and P.K. Liaw, Mechanical Behavior of High-Entropy Alloys, *Prog. Mater. Sci.*, 2021, **118**, 100777. <https://doi.org/10.1016/j.pmatsci.2021.100777>
- S. Zhao, Z. Li, C. Zhu, W. Yang, Z. Zhang, D.E.J. Armstrong, P.S. Grant, R.O. Ritchie and M.A. Meyers, Amorphization in Extreme Deformation of the CrMnFeCoNi High-Entropy Alloy, *Sci. Adv.*, 2021, **7**, p 3108. <https://doi.org/10.1126/sciadv.abb3108>
- H. Xiang, Y. Xing, F.-Z. Dai, H. Wang, L. Su, L. Miao, G. Zhang, Y. Wang, X. Qi, L. Yao, H. Wang, B. Zhao, J. Li and Y. Zhou, High-Entropy Ceramics: Present Status, Challenges, and a Look Forward, *Adv. Ceram.*, 2021, **10**, p 385–441. <https://doi.org/10.1007/s40145-021-0477-y>
- O.V. Dudnik, S.M. Lakiza, I.M. Grechanyuk, V.P. Red'ko, M.S. Glabay, V.B. Shmibelsky, I.O. Marek, A.K. Ruban and M.I. Grechanyuk, High-Entropy Ceramics for Thermal Barrier Coatings Produced from ZrO₂ Doped with Rare-Earth Metal Oxides, *Powder Metall. Met. Ceram.*, 2021, **59**, p 556–563. <https://doi.org/10.1007/s11106-021-00187-4>
- P. Asghari-Rad, N.T.-C. Nguyen, Y. Kim, A. Zargaran, P. Sathiyamoorthi and H.S. Kim, TiC-Reinforced CoCrFeMnNi Composite Processed by Cold-Consolidation and Subsequent Annealing, *Mater. Lett.*, 2021, **303**, 130503. <https://doi.org/10.1016/j.matlet.2021.130503>
- R. Nikbakht, S.H. Seyedein, S. Kheirandish, H. Assadi and B. Jodoin, Asymmetrical Bonding in Cold Spraying of Dissimilar Materials, *Appl. Surf. Sci.*, 2018, **444**, p 621–632. <https://doi.org/10.1016/j.apsusc.2018.03.103>
- R. Nikbakht, S.H. Seyedein, S. Kheirandish, H. Assadi and B. Jodoin, The Role of Deposition Sequence in Cold Spraying of Dissimilar Materials, *Surf. Coat. Technol.*, 2019, **367**, p 75–85. <https://doi.org/10.1016/j.surfcoat.2019.03.065>
- R. Nikbakht, H. Assadi and B. Jodoin, Intermetallic Phase Evolution of Cold-Sprayed Ni-Ti Composite Coatings: Influence of As-Sprayed Chemical Composition, *J. Therm. Spray Technol.*, 2021, **30**, p 119–130. <https://doi.org/10.1007/s11666-020-01112-8>
- R. Nikbakht, M. Saadati, H. Assadi, K. Jahani and B. Jodoin, Dynamic Microstructure Evolution in Cold Sprayed NiTi Composite Coatings, *Surf. Coat. Technol.*, 2021, **421**, 127456. <https://doi.org/10.1016/j.surfcoat.2021.127456>
- R. Nikbakht, H. Assadi, K. Jahani, M. Saadati and B. Jodoin, Cold Spray Deformation and Deposition of Blended Feedstock Powders Not Necessarily Obey the Rule of Mixture, *Surf. Coat. Technol.*, 2021, **424**, 127644. <https://doi.org/10.1016/j.surfcoat.2021.127644>
- R. Dykhuizen, M. Smith, D. Gilmore, R. Neiser, X. Jiang and S. Sampath, Impact of High Velocity Cold Spray Particles, *J. Therm. Spray Technol.*, 1999, **8**, p 559–564.
- R.C. Dykhuizen and M.F. Smith, Gas Dynamic Principles of Cold Spray, *J. Therm. Spray Technol.*, 1998, **7**, p 205–212. <https://doi.org/10.1361/105996398770350945>
- A. Papyrin, V. Kosarev, S. Klinkov, A. Alkimov, V. Fomin, Chapter 2 - High-Velocity Interaction of Particles with the Substrate. Experiment and Modeling, *Cold Spray Technology*, Elsevier, Oxford, 2007, pp. 33–118, <https://doi.org/10.1016/B978-008045155-8/50002-8>.
- V.F. Kosarev, S.V. Klinkov, A.P. Alkhimov and A.N. Papyrin, On some Aspects of Gas Dynamics of the Cold Spray Process, *J. Therm. Spray Technol.*, 2003, **12**, p 265–281. <https://doi.org/10.1361/105996303770348384>
- H. Assadi, F. Gärtner, T. Stoltenhoff and H. Kreye, Bonding Mechanism in Cold Gas Spraying, *Acta Mater.*, 2003, **51**, p 4379–4394. [https://doi.org/10.1016/S1359-6454\(03\)00274-X](https://doi.org/10.1016/S1359-6454(03)00274-X)
- H. Assadi, T. Schmidt, H. Richter, J.-O. Kliemann, K. Binder, F. Gärtner, T. Klassen and H. Kreye, On Parameter Selection in Cold Spraying, *J. Therm. Spray Technol.*, 2011, **20**, p 1161–1176. <https://doi.org/10.1007/s11666-011-9662-9>
- L. Ajdelsztajn, J.M. Schoenung, B. Jodoin and G.E. Kim, Cold Spray Deposition of Nanocrystalline Aluminum Alloys, *Metall. Mater. Trans. A*, 2005, **36**, p 657–666. <https://doi.org/10.1007/s11661-005-0099-y>
- P. Richer, B. Jodoin and L. Ajdelsztajn, Substrate Roughness and Thickness Effects on Cold Spray Nanocrystalline Al–Mg Coatings, *J. Therm. Spray Technol.*, 2006, **15**, p 246–254. <https://doi.org/10.1361/105996306X108174>
- R. Ghelichi, D. MacDonald, S. Bagherifard, H. Jahed, M. Gualiano and B. Jodoin, Microstructure and Fatigue Behavior of Cold Spray Coated Al5052, *Acta Mater.*, 2012, **60**, p 6555–6561. <https://doi.org/10.1016/j.actamat.2012.08.020>
- S. Rech, A. Trentin, S. Vezzù, E. Vedelago, J.-G. Legoux and E. Irissou, Different Cold Spray Deposition Strategies: Single- and Multi-layers to Repair Aluminium Alloy Components, *J. Therm. Spray Technol.*, 2014, **23**, p 1237–1250. <https://doi.org/10.1007/s11666-014-0141-y>

26. B. Al-Mangour, R. Mongrain, E. Irissou and S. Yue, Improving the Strength and Corrosion Resistance of 316L Stainless Steel for Biomedical Applications Using Cold Spray, *Surf. Coat. Technol.*, 2013, **216**, p 297–307. <https://doi.org/10.1016/j.surfcoat.2012.11.061>
27. X. Meng, J. Zhang, J. Zhao, Y. Liang and Y. Zhang, Influence of Gas Temperature on Microstructure and Properties of Cold Spray 304SS Coating, *J. Mater. Sci. Technol.*, 2011, **27**, p 809–815. [https://doi.org/10.1016/S1005-0302\(11\)60147-3](https://doi.org/10.1016/S1005-0302(11)60147-3)
28. X.-M. Meng, J.-B. Zhang, W. Han, J. Zhao and Y.-L. Liang, Influence of Annealing Treatment on the Microstructure and Mechanical Performance of Cold Sprayed 304 Stainless Steel Coating, *Appl. Surf. Sci.*, 2011, **258**, p 700–704. <https://doi.org/10.1016/j.apsusc.2011.07.107>
29. L.N. Brewer, J.F. Schiel, E.S.K. Menon and D.J. Woo, The Connections Between Powder Variability and Coating Microstructures for Cold Spray Deposition of Austenitic Stainless Steel, *Surf. Coat. Technol.*, 2018, **334**, p 50–60. <https://doi.org/10.1016/j.surfcoat.2017.10.082>
30. H. Yeom, T. Dabney, N. Pocquette, K. Ross, F.E. Pfefferkorn and K. Sridharan, Cold Spray Deposition of 304L Stainless Steel to Mitigate Chloride-Induced Stress Corrosion Cracking in Canisters for Used Nuclear Fuel Storage, *J. Nucl. Mater.*, 2020, **538**, 152254. <https://doi.org/10.1016/j.jnucmat.2020.152254>
31. G. Mauer, R. Singh, K.-H. Rauwald, S. Schrüfer, S. Wilson and R. Vaßen, Diagnostics of Cold-Sprayed Particle Velocities Approaching Critical Deposition Conditions, *J. Therm. Spray Technol.*, 2017, **26**, p 1423–1433. <https://doi.org/10.1007/s11666-017-0596-8>
32. S. Yin, W. Li, B. Song, X. Yan, M. Kuang, Y. Xu, K. Wen and R. Lupoi, Deposition of FeCoNiCrMn High Entropy Alloy (HEA) Coating Via Cold Spraying, *J. Mater. Sci. Technol.*, 2019, **35**, p 1003–1007. <https://doi.org/10.1016/j.jmst.2018.12.015>
33. Y. Xu, W. Li, L. Qu, X. Yang, B. Song, R. Lupoi and S. Yin, Solid-State Cold Spraying of FeCoCrNiMn High-Entropy Alloy: An Insight into Microstructure Evolution and Oxidation Behavior at 700–900 °C, *J. Mater. Sci. Technol.*, 2021, **2021**(68), p 172–183. <https://doi.org/10.1016/j.jmst.2020.06.041>
34. J.-E. Ahn, Y.-K. Kim, S.-H. Yoon and K.-A. Lee, Tuning the Microstructure and Mechanical Properties of Cold Sprayed Equiatomic CoCrFeMnNi High-Entropy Alloy Coating Layer, *Met Mater. Int.*, 2021, **27**, p 2406–2415. <https://doi.org/10.1007/s12540-020-00886-4>
35. R. Nikbakht, M. Saadati, T.-S. Kim, M. Jahazi, H.S. Kim and B. Jodoin, Cold Spray Deposition Characteristic and Bonding of CrMnCoFeNi High Entropy Alloy, *Surf. Coat. Technol.*, 2021, **425**, 127748. <https://doi.org/10.1016/j.surfcoat.2021.127748>
36. T. Schmidt, F. Gärtner, H. Assadi and H. Kreye, Development of a Generalized Parameter Window for Cold Spray Deposition, *Acta Mater.*, 2006, **54**, p 729–742. <https://doi.org/10.1016/j.actamat.2005.10.005>
37. D.K. Christoulis, M. Jeandin, E. Irissou, J.-G. Legoux, W. Knapp, D. Dumitras, Laser-Assisted Cold Spray (LACS), InTech, Rijeka, Croatia, 2012, p 59–96.
38. R. Ortiz-Fernandez and B. Jodoin, Hybrid Additive Manufacturing Technology: Induction Heating Cold Spray—Part I: Fundamentals of Deposition Process, *J. Therm. Spray Technol.*, 2020, **29**, p 684–699. <https://doi.org/10.1007/s11666-020-01005-w>
39. D.J. Barton, V.S. Bhattiprolu, G.B. Thompson and L.N. Brewer, Laser Assisted Cold Spray of AISI 4340 Steel, *Surf. Coat. Technol.*, 2020, **400**, 126218. <https://doi.org/10.1016/j.surfcoat.2020.126218>
40. M. Perton, S. Costil, W. Wong, D. Poirier, E. Irissou, J.G. Legoux, A. Blouin and S. Yue, Effect of Pulsed Laser Ablation and Continuous Laser Heating on the Adhesion and Cohesion of Cold Sprayed Ti-6Al-4V Coatings, *J. Therm. Spray Technol.*, 2021, **21**, p 1322–1333. <https://doi.org/10.1007/s11666-012-9812-8>
41. C.V. Cojocar, M. Aghasibeig, E. Irissou, MCrAlX (X = Y, Hf and Si) Bond Coats by Cold Spray for High Temperature Applications, 2021, **83881**, p 36–43. <https://doi.org/10.31399/asm.ep.itsc2021p0036>
42. D. Yim, M.J. Jang, J.W. Bae, J. Moon, C.-H. Lee, S.-J. Hong, S.I. Hong and H.S. Kim, Compaction Behavior of Water-Atomized CoCrFeMnNi High-Entropy Alloy Powders, *Mater. Chem. Phys.*, 2018, **210**, p 95–102. <https://doi.org/10.1016/j.matchemphys.2017.06.013>
43. H. Kriaa, A. Guitton, N. Maloufi., Fundamental and Experimental Aspects of Diffraction for Characterizing Dislocations by Electron Channeling Contrast Imaging in Scanning Electron Microscope. *Sci. Rep.*, 2017, **7**, 9742–9749. <https://doi.org/10.1038/s41598-017-09756-3>
44. D. Poirier, J.-G. Legoux, P. Vo, B. Blais, J.D. Giallonardo and P.G. Keech, Powder Development and Qualification for High-Performance Cold Spray Copper Coatings on Steel Substrates, *J. Therm. Spray Technol.*, 2019, **28**, p 444–459. <https://doi.org/10.1007/s11666-019-00833-9>
45. R.A. Seraj, A. Abdollah-zadeh, S. Dosta, H. Canales, H. Assadi and I.G. Cano, The Effect of Traverse Speed on Deposition Efficiency of Cold Sprayed Stellite 21, *Surf. Coat. Technol.*, 2019, **366**, p 24–34. <https://doi.org/10.1016/j.surfcoat.2019.03.012>
46. J. Moon, S.I. Hong, J.B. Seol, J.W. Bae, J.M. Park and H.S. Kim, Strain-Rate Sensitivity of High-Entropy Alloys and Its Significance in Deformation, *Mater. Res. Lett.*, 2019, **7**, p 503–509. <https://doi.org/10.1080/21663831.2019.1668489>
47. H. Shahmir, P. Asghari-Rad, M.S. Mehranpour, F. Forghani, H.S. Kim and M. Nili-Ahmadabadi, Evidence of FCC to HCP and BCC-Martensitic Transformations in a CoCrFeNiMn High-Entropy Alloy by Severe Plastic Deformation, *Mater. Sci. Eng. A*, 2021, **807**, 140875. <https://doi.org/10.1016/j.msea.2021.140875>
48. R. Nikbakht, M. Saadati, M. Jahazi, H. Assadi and B. Jodoin, *EBSD Analysis Enhancement of Cold Sprayed Composite Materials: Sample Preparation, Annealing, and Scan Optimization*, Microscopical Society Symposium of Canada, Université de Sherbrooke, Québec, Canada, 2020.
49. Z. Li, S. Zhao, S.M. Alotaibi, Y. Liu, B. Wang and M.A. Meyers, Adiabatic Shear Localization in the CrMnFeCoNi High-Entropy Alloy, *Acta Mater.*, 2018, **151**, p 424–431. <https://doi.org/10.1016/j.actamat.2018.03.040>
50. G. Strnad and L. Jakab-Farkas, Improving the Accuracy of Low-Load Vickers Microhardness Testing of Hard Thin Films, *Proc. Technol.*, 2014, **12**, p 289–294. <https://doi.org/10.1016/j.protcy.2013.12.488>
51. A.R. Bushroa, R.G. Rahbari, H.H. Masjuki and M.R. Muhamad, Approximation of Crystallite Size and Microstrain via XRD Line Broadening Analysis in TiSiN Thin Films, *Vacuum*, 2012, **86**, p 1107–1112. <https://doi.org/10.1016/j.vacuum.2011.10.011>
52. Z. Liu, H. Wang, M.J.R. Haché, X. Chu, E. Irissou and Y. Zou, Prediction of Heterogeneous Microstructural Evolution in Cold-Sprayed Copper Coatings Using Local Zener-Hollomon Parameter and Strain, *Acta Mater.*, 2020, **193**, p 191–201. <https://doi.org/10.1016/j.actamat.2020.04.041>

Publisher's Note Springer Nature remains neutral with regard to jurisdictional claims in published maps and institutional affiliations.